

# Tuning the thermal conductivity of a silicon membrane using nanopillars: From crystalline to amorphous pillars

Lina Yang<sup>1,\*</sup>, Yixin Xu<sup>2</sup>, Xianheng Wang<sup>1</sup>, and Yanguang Zhou<sup>2,3,†</sup>

<sup>1</sup>*School of Aerospace Engineering, Beijing Institute of Technology, Beijing 100081, China*

<sup>2</sup>*Department of Mechanical and Aerospace Engineering, The Hong Kong University of Science and Technology, Clear Water Bay, Kowloon, Hong Kong SAR, China*

<sup>3</sup>*HKUST Shenzhen-Hong Kong Collaborative Innovation Research Institute, Futian, Shenzhen, Guangdong, China*



(Received 10 April 2024; revised 6 August 2024; accepted 14 August 2024; published 9 September 2024)

Tuning thermal transport in nanostructures is essential for many applications, such as thermal management and thermoelectrics. Nanophononic metamaterials (NPMs) have shown great potential for reducing thermal conductivity. In this work, the thermal conductivity of NPMs with crystalline Si (*c*-Si) pillar, crystalline Ge (*c*-Ge) pillar, and amorphous Si (*a*-Si) pillar are systematically investigated by a molecular dynamics method. An analysis of phonon dispersion and spectral energy density shows that phonon dispersions of a Si membrane are flattened due to local resonant hybridization induced by both crystalline and amorphous pillars. In addition, an *a*-Si pillar can cause a larger reduction in thermal conductivity compared with a *c*-Si pillar. Specifically, when the atomic mass of the atoms in the pillars increases, the thermal conductivity of NPMs with a crystalline pillar increases because of the weakened phonon hybridization. However, the thermal conductivity of NPMs with an amorphous pillar is almost unchanged. The analyses of the reduction of thermal conductivity show that both resonant hybridization and scattering mechanisms are important in NPMs with a crystalline pillar, while the scattering mechanism dominates in NPMs with an amorphous pillar and NPMs with a short crystalline pillar. The results of this work can provide meaningful insights into controlling thermal transport in NPMs by choosing the materials and atomic mass of pillars for specific applications.

DOI: 10.1103/PhysRevApplied.22.034016

## I. INTRODUCTION

Controlling thermal transport in nanostructures has attracted significant attention in recent years due to its promising applications such as thermal management [1,2] and thermoelectric energy conversion [3–5]. For instance, in the pursuit of high-efficiency thermoelectrics, a promising avenue of the strategies lies in the development of nanophononic metamaterials (NPMs) with low thermal conductivity ( $\kappa$ ) [6–8]. NPMs enable phonon resonant hybridizations between the vibrational modes of nanoresonators and the phonon modes of the host medium, leading to enhanced control over thermal conductivity [9–12]. Meanwhile, previous studies found that the pillared silicon (Si) membrane can reduce  $\kappa$  by two orders of magnitudes [9,13]. Unlike nanoscale phononic crystals [14,15], NPMs do not require periodicity in the arrangement of resonators to achieve resonant hybridizations, which renders NPMs highly robust to disorder in the arrangement of resonators [9]. Additionally, as the resonators of NPMs

are located outside the membrane [7,13,16], electron transport in these materials remains almost unaffected, which is highly desirable for developing high-efficiency thermoelectrics.

Substantial efforts have been aimed at comprehending the thermal transport properties of NPMs and the underlying mechanisms since the NPM was investigated by Davis and Hussein in 2014 [6]. For instance, Anufriev *et al.* found that the  $\kappa$  of nanobeams with aluminum (Al) nanopillar is about 20% smaller compared with the pristine nanobeams, which is mainly caused by phonon scatterings at the pillar and beam interface due to the intermixing of Al and Si atoms [17]. Maire *et al.* showed that the cross-sections control the  $\kappa$  of nanowires with fishbone nanostructures, and the periodic wings further reduce  $\kappa$  [18]. Later analyses found that the reduction of  $\kappa$  is mainly caused by the periodicity of wings, which can flatten the phonon dispersions rather than by local resonances [19]. By conducting atomistic modeling and experiments, Neogi *et al.* found that the reduction of  $\kappa$  in ultrathin-suspended silicon membranes is mainly controlled by surface scatterings because the rough layers of native oxide at surfaces limit the mean free path of thermal phonons below 100 nm

\*Contact author: yangln@bit.edu.cn

†Contact author: maeyzhou@ust.hk

[20]. Similarly, Huang *et al.* reported that the  $\kappa$  of suspended silicon membranes with nanopillars is controlled by incoherent phonon scatterings that causes less than 16% reduction of  $\kappa$ , which is examined by comparing the results of Monte Carlo simulation and experimental measurements [21]. Recently, the device-scale suspended silicon membranes with GaN nanopillars were fabricated, and experimental measurements found that the nanopillars cause up to 21% reduction of  $\kappa$ ; meanwhile, the power factor remains unaffected [16]. The effect of rough surface (sawtooth-shaped surface and square-shaped surface), amorphous surface, and smooth surface on phonon reflection were studied by atomistic wave-packet simulations [22]. It is found that the reflected wave-packet distribution does not follow the well-known Ziman model but shows a nonmonotonic dependence on the depth of the surface roughness, while the amorphous surface can absorb the incident wave packet and then reflect it diffusively.

Besides these experimental works, different types of NPMs have been studied theoretically. Xiong *et al.* found that combining a designed resonant structure with alloying can lead to extremely low  $\kappa$  in Si nanowires, because the local resonances greatly reduce the phonon group velocities and mean free paths in the low-frequency ( $< 4$  THz) range; concurrently, alloy scatterings impede high-frequency phonons [7]. Later, Zhang *et al.* designed a Si nanowire with a helical wall, which is more effective in reducing  $\kappa$  compared with straight nanowalls and nanopillars. They demonstrated the resonant hybridization and mode localization in the helical walls by analyzing the phonon dispersions and phonon spatial distributions, respectively [23]. Further, it was found that introducing imperfections such as vacancy defects, mass mismatch, and alloy disorder in the pillars can weaken the local resonant hybridization, leading to a higher  $\kappa$  compared with that of the pristine NPMs [24,25]. For instance, the  $\kappa$  of pillared graphene nanoribbon (GNR) is increased from  $\sim 47$  W/(m K) to  $\sim 63$  W/(m K) by increasing the atomic mass of atoms in pillars [24]. Although previous works have reported that introducing nanopillars affects  $\kappa$  through several mechanisms [11], such as local resonance [13], phonon interference due to pillar periodicity [19], and diffuse phonon scatterings [17,20,21], tuning the  $\kappa$  of the NPMs by designing different kinds of resonators is less investigated and the corresponding phonon transport behaviors remain unclear.

In this work, the effect of the crystalline Si (*c*-Si) pillar, amorphous Si (*a*-Si) pillar, and crystalline Ge (*c*-Ge) pillar on regulating the  $\kappa$  of a Si membrane is investigated by equilibrium molecular dynamics simulations (EMD). In addition, the mass of atoms in pillars is tuned to manipulate the  $\kappa$  of NPMs with *c*-Si and *a*-Si pillars. The phonon local resonant hybridizations in NPMs are systematically analyzed by calculating phonon dispersions and spectral energy distribution (SED). Furthermore, the spectral

thermal conductivity is also quantified. The results of our work are expected to provide insights into the interplay between the resonators of NPMs and phonon transport.

## II. MODEL AND METHOD

To study the  $\kappa$  of the NPMs, the Si membrane with a *c*-Si pillar, a *c*-Ge pillar, and an *a*-Si pillar, as shown in Fig. 1(a), are created; these are noted as Type 3, Type 2, and Type 4, respectively. When the atomic mass of atoms in the *c*-Si pillar is changed to  $M$  in units of amu, it is noted as the *c*-Si $^M$  pillar. The NPM with *c*-Si $^M$  pillar is represented by Type 1. Here, the atomic mass of Si and Ge atoms is denoted by MSi and MGe, respectively. If  $M$  equals MSi, the *c*-Si $^M$  pillar represents the *c*-Si pillar. In Figs. 1(b) and 1(c), the value of  $M$  is set at MGe for Type 1. In addition,  $L_a = 5.43$  Å and  $L_{Ge} = 5.66$  Å are the lattice constant of bulk Si and Ge, respectively. The unit cell of the Si membrane is  $6L_a \times 6L_a \times 6L_a$ , the size of the *c*-Ge pillar is  $4L_{Ge} \times 4L_{Ge} \times 6L_{Ge}$ , and the size of other pillars is  $4L_a \times 4L_a \times 6L_a$ . The images of the system structures are created with OVITO [26], version 2.9.0, in this paper.

The thermal conductivity of the NPM is calculated using the EMD method. In the simulations, the periodic boundary condition is applied in the *x*- and *y*-direction and the free boundary condition is applied in the *z*-direction. The Tersoff potential is used to describe the interaction between Si atoms [27] and Ge atoms. The couplings between Si and Ge atoms are obtained by following the combination rule [27], which has been applied to describe the Si and the SiC system. All molecular dynamics simulations are performed using LAMMPS (large-scale atomic or molecular massively parallel simulator) [28], and the temperature is set at 300 K. The thermal conductivity is calculated from the Green-Kubo formula [29], i.e.,

$$\kappa = \frac{1}{2Vk_B T^2} \int_0^\infty \langle J(0) \cdot J(\tau) \rangle d\tau, \quad (1)$$

where  $k_B$  is the Boltzmann constant,  $V$  is the system volume,  $T$  is the temperature, and  $J$  is the heat current. The time step in the EMD simulations is set at 0.5 fs. Firstly, the NPM system is equilibrated at 300 K using a canonical ensemble with a Langevin heat reservoir for  $6 \times 10^5$  steps (300 ps). Then, the heat current is recorded at each step during the EMD simulations under a microcanonical ensemble (NVE) for  $8 \times 10^6$  steps (4 ns). In this work, the time averaging supplemented by 20 simulation cases with different initial conditions is used to calculate the thermal conductivity, which has been used in many research studies [29–31], and the statistical errors are obtained by calculating the standard deviation.

The *a*-Si pillar is obtained using the melt-quenching method [32–35]. Initially, the Si membrane with the *c*-Si

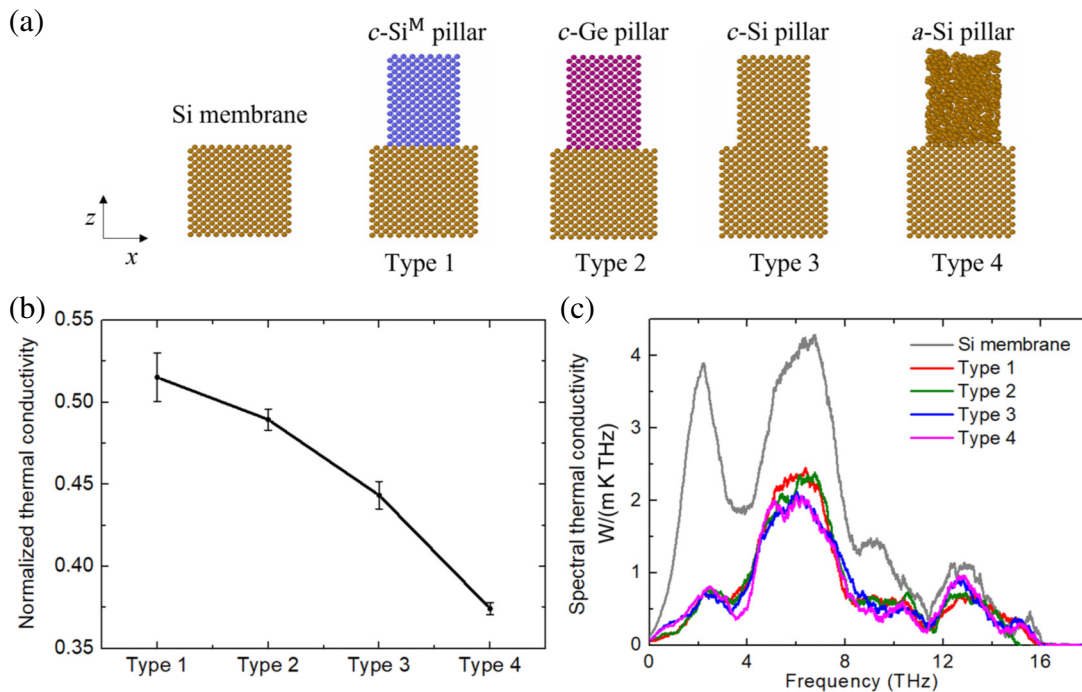


FIG. 1. (a) Structure of the Si membrane, the NPM with the  $c\text{-Si}^M$  pillar (Type 1), the NPM with the  $c\text{-Ge}$  pillar (Type 2), the NPM with the  $c\text{-Si}$  pillar (Type 3), and the NPM with the  $a\text{-Si}$  pillar (Type 4). (b) Normalized thermal conductivity of the NPM from Type 1 to Type 4. The  $\kappa$  of the NPM is normalized by the  $\kappa$  of the Si membrane. (c) Spectral thermal conductivity of the Si membrane and the NPMs versus frequency. In (b) and (c), the value of  $M$  is set at MGe for Type 1.

pillar is created. The atoms in the Si membrane are fixed, and the atoms in the  $c\text{-Si}$  pillar are melted at 3600 K by a Nosé-Hoover thermostat for 0.5 ns, then the pillar is quickly quenched to 1000 K at the rate of 860 K/ps. Finally, the atoms in the pillar are annealed at 1000 K for 0.5 ns, then quickly quenched to 20 K at the rate of 160 K/ps. To determine the atomic configuration of the  $a\text{-Si}$  pillar, an equilibration simulation is first performed for the  $a\text{-Si}$  pillar for 2.5 ns in an  $NVT$  ensemble, and then the steady atomic positions are calculated by averaging the time-dependent atomic positions during the next 2.5 ns.

To characterize phonon transport in the NPMs, the phonon dispersions of the NPMs and Si membranes are calculated using lattice dynamics implemented in GULP [36]. The SED [37–39] is directly obtained from the MD simulations by recording the velocities of atoms. The SED expression  $\Phi'$  is given by

$$\Phi'(k, \omega) = \frac{1}{4\pi\tau_0} \sum_{\alpha}^3 \sum_{b=1}^n \frac{m_b}{N} \left| \sum_1^N \int_0^{\tau_0} \dot{u}_{\alpha}(l, b, t) \exp(\Theta dt) \right|^2, \quad (2)$$

where  $\dot{u}_{\alpha}$  is the  $\alpha$ th component of the velocity of the  $b$ th atom in the  $l$ th unit cell at time  $t$  and  $\Theta = i[\vec{k} \cdot \vec{r}_0(l, b) - \omega t]$ ;  $m_b$  is the mass of the  $b$ th atom,  $\tau_0$  is the simulation time,  $\vec{r}_0$  is the equilibrium position vector of the  $l$ th unit cell, and  $\omega$  is the angular frequency. Here,

the units of  $\Phi'$  is J ps. Moreover,  $N$  is the total number of unit cells and  $n$  is the number of atoms in the unit cell. In the SED analyses, the supercell of the NPM consists of 40 unit cells in the  $x$ -direction and a unit cell in the  $y$ - and  $z$ -direction. Here, the MD simulations are performed at 300 K for  $2 \times 10^6$  timesteps to extract the atomic velocities.

To quantify the spectral phonon transmission function, we further calculate the spectral thermal conductivity using nonequilibrium molecular dynamics simulations (NEMD), in which the spectral heat current can be calculated with [40,41]

$$Q(\omega) = 2 \sum_{i \in \text{left}} \sum_{j \in \text{right}} \text{Re} \left[ \int_{-\infty}^{+\infty} \left\langle \frac{\partial U_j}{\partial \vec{r}_i} \right\rangle_{\tau} \vec{v}_i(0) - \left\langle \frac{\partial U_i}{\partial \vec{r}_j} \right\rangle_{\tau} \vec{v}_j(0) \right] e^{-i\omega\tau} d\tau, \quad (3)$$

where  $U_j$  is the potential energy of atom  $j$ ,  $\vec{v}_i$  is the velocity of atom  $i$ , and the brackets  $\langle \rangle$  denote the time average in the MD simulations. The atomic velocities  $\vec{v}_i$  and the atomic potential partial function  $\partial U_j / \partial \vec{r}_i$  are updated every 20 steps, i.e., every 10 fs. The size effects and the configuration of the NEMD simulations are shown in Fig. S5 in the Supplemental Material [42]. Afterward, by assuming the same temperature gradient  $\nabla T$  over all the phonons, the spectral thermal conductivity is then calculated via

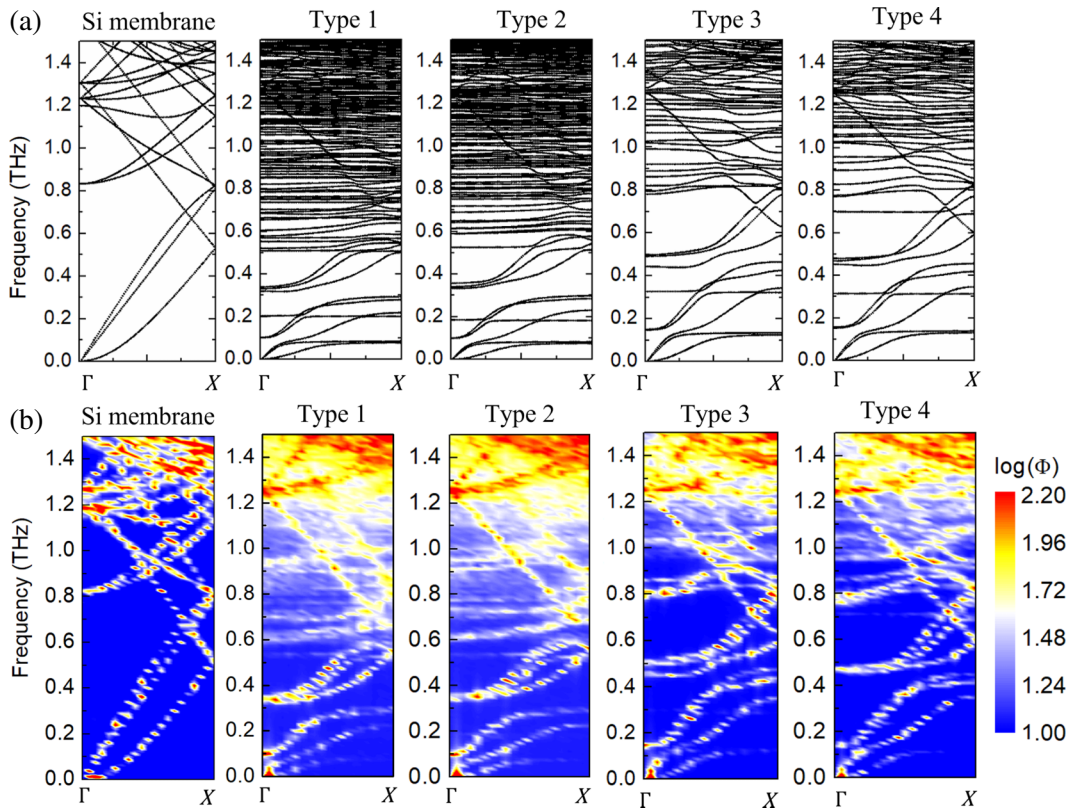


FIG. 2. (a) Phonon dispersions of the Si membrane and the NPMs calculated by lattice dynamics. (b) SED spectrum of the Si membrane and the NPMs when only considering atoms in the Si membrane. The meaning of Type 1 to Type 4 is the same as in Fig. 1.

Fourier's law, i.e.,  $\kappa(\omega) = Q(\omega)/A\nabla T$  in which  $A$  denotes the system cross-section area and  $\nabla T$  is the temperature gradient along the in-plane direction.

### III. RESULTS

#### A. Thermal conductivity of NPMs

The thermal conductivity of the NPMs in Fig. 1(a) is calculated using the EMD method through Eq. (1). In Figs. 1(b) and 1(c), the value of  $M$  is set at MGe for the  $c\text{-Si}^M$  pillar in Type 1. For comparison, the thermal conductivity of the bulk Si and Si membranes in Fig. 1(a) is also computed. The simulation cell of the bulk Si is set at  $6L_a \times 6L_a \times 6L_a$  with periodic boundary conditions in all three spatial directions to overcome the size effect [29,43,44]. The calculated  $\kappa$  is  $238.4 \pm 3.6$  W/(m K) and  $40.6 \pm 0.6$  W/(m K) for the bulk Si and Si membrane at 300 K, respectively, which is consistent with the prediction in refs. [20] and [45]. The thermal conductivity as a function of time is shown in Fig. S1 in the Supplemental Material [42]. The thermal conductivity of the Si membrane calculated using the NEMD method is 28.19 W/(m K) at  $T=300$  K, as shown in Fig. S5 in the Supplemental Material [42], which is also higher than experimental results (i.e.,  $\sim 10$  W/(m K) for a membrane with a thickness of  $\sim 10$  nm [46]). It is noted that there

exists a gap between the MD results and the experimental measurements [47], which can be caused by the intrinsic phonon distribution and the accuracy of empirical potentials. On one hand, all the vibrational modes are assumed to be fully occupied in the MD simulations; they follow the classical limit of Boltzmann distributions [48] and, as a result, the MD simulations overestimate the heat capacity and the corresponding thermal conductivities. On the other hand, the accuracy of the MD results strongly relies on the empirical potential. Here, the popular potential for the Si (Ge) systems [27] is applied, which has been widely used to study thermal transport in Si-based materials, including the bulk Si [29], Si/Ge superlattices [49], and Si membranes [50]. However, this discrepancy will not severely affect the comparison of the NPMs and Si membranes since the same simulation methods are used, and the fundamental mechanisms should be independent of the potential. The  $\kappa$  of the NPMs is normalized by the  $\kappa$  of the Si membrane, which is shown in Fig. 1(b). The normalized  $\kappa$  of the NPM with the  $c\text{-Si}^M$  and  $c\text{-Ge}$  pillars is larger than that of the NPM with the  $c\text{-Si}$  pillar, while  $a\text{-Si}$  pillar has a stronger effect on the reduction of  $\kappa$  compared with the  $c\text{-Si}$  pillar.

To further understand the reduction of the  $\kappa$  of the NPMs in Fig. 1(b), the spectral  $\kappa$  [Fig. 1(c)] is investigated. Compared with the Si membrane, the spectral  $\kappa$  of the NPMs is reduced in a wide range of frequencies from 0 to 14 THz.

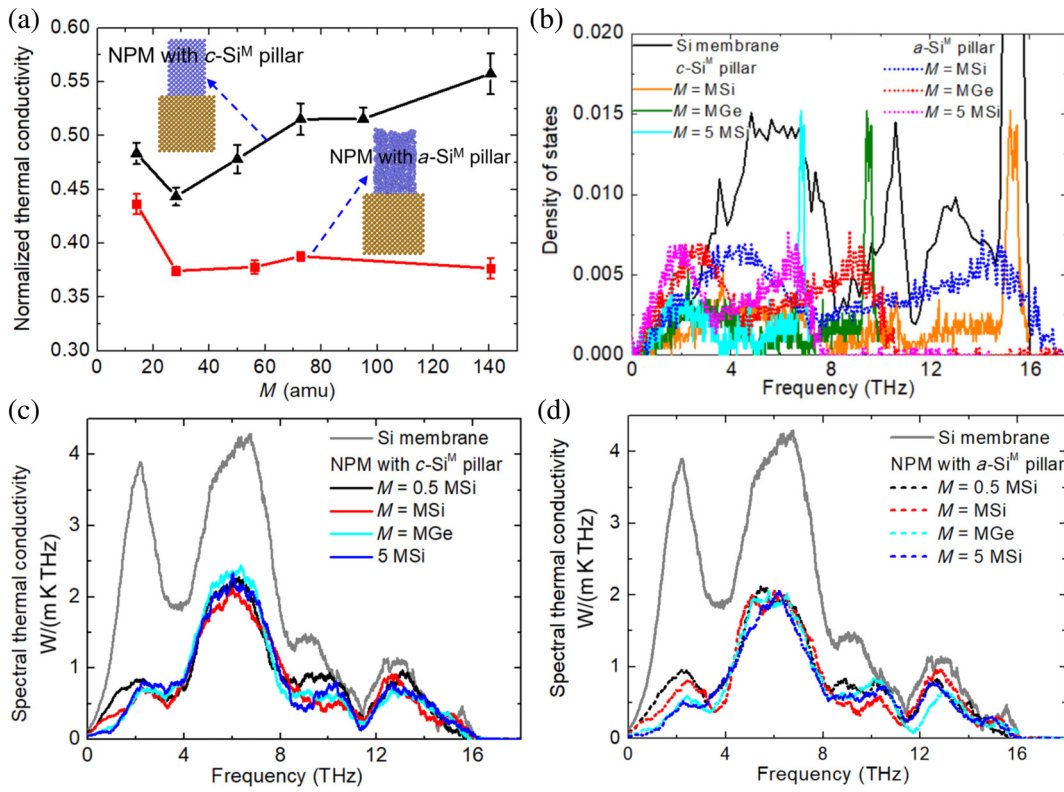


FIG. 3. (a) Normalized thermal conductivity of the NPM with the  $c\text{-Si}^M$  and  $a\text{-Si}^M$  pillars versus the value of  $M$ . Here, when the atomic mass of the atoms in the pillars is changed to  $M$  (in units of amu), it is denoted as the  $c\text{-Si}^M$  and  $a\text{-Si}^M$  pillars. The thermal conductivity of the NPM is normalized by the  $\kappa$  of the Si membrane. (b) Density of states (DOS) versus frequency for the  $c\text{-Si}^M$  and  $a\text{-Si}^M$  pillars. (c) Spectral thermal conductivity of the NPM with the  $c\text{-Si}^M$  pillar. (d) Spectral thermal conductivity of the NPM with the  $a\text{-Si}^M$  pillar.

At the low-frequency range ( $< 2.0$  THz), the  $c\text{-Si}^M$  and  $c\text{-Ge}$  pillars cause slightly smaller spectral  $\kappa$  compared with the  $c\text{-Si}$  pillar. However, from 5 to 7.5 THz, the NPMs with the  $c\text{-Si}^M$  and  $c\text{-Ge}$  pillars have larger spectral  $\kappa$ , which leads to the larger  $\kappa$  compared with the NPM with the  $c\text{-Si}$  pillar. Furthermore, the contribution of the low-frequency phonons ( $< 2.0$  THz) to spectral  $\kappa$  is almost equivalent in the  $a\text{-Si}$ -pillared NPM and the  $c\text{-Si}$ -pillared NPM. However, the spectral  $\kappa$  of the NPM with the  $a\text{-Si}$  pillar is smaller for frequencies ranging from 3.5 to 4.5 THz and 7.5 to 10 THz, which leads to the smaller  $\kappa$  compared with the NPM with the  $c\text{-Si}$  pillar.

It was reported that the phonon hybridization between the host medium and the resonant surface structures played an essential role in reducing the thermal conductivity of nanostructures [7, 19, 25]. Here, the phonon hybridizations in the NPMs are analyzed by calculating their phonon dispersion using the lattice dynamics method implemented in GULP [36], as shown in Fig. 2(a). In addition, the SED spectrum of the Si membrane and the Si membrane in the NPMs, as shown in Fig. 2(b), are also calculated. The SED spectrum of the NPMs, considering all atoms in the

system, is shown in Fig. S2 in the Supplemental Material [42]. Since the phonon modes with high frequency are difficult to distinguish in the SED spectrum, we only consider the low-frequency phonon modes ( $\leq 1.5$  THz) here. The results show that introducing the nanopillars can affect the low-frequency phonon modes of the Si membrane; for example, the first resonant hybridization causing the flattened bands occurs at  $\sim 0.1$  THz for Type 1 and Type 2 NPMs and at  $\sim 0.15$  THz for Type 3 and Type 4 NPMs, which leads to a reduction of the  $\kappa$  of the NPM compared with the pure Si membrane. In addition, the phonon dispersions of Type 1 and Type 3 are close to that of Type 2 and Type 4, respectively. However, the lattice mismatch at the interface between the  $c\text{-Ge}$  pillar and the Si membrane causes stronger phonon scatterings. Therefore, the NPM with the  $c\text{-Ge}$  pillar can have a smaller  $\kappa$  compared to the NPM with the  $c\text{-Si}^M$  pillar. Similarly, the roughness of the amorphous pillar also causes stronger phonon scatterings at the interface between the  $a\text{-Si}$  pillar and Si membrane; thus, the NPM with the  $a\text{-Si}$  pillar can have a smaller  $\kappa$  than the NPM with the  $c\text{-Si}$  pillar.

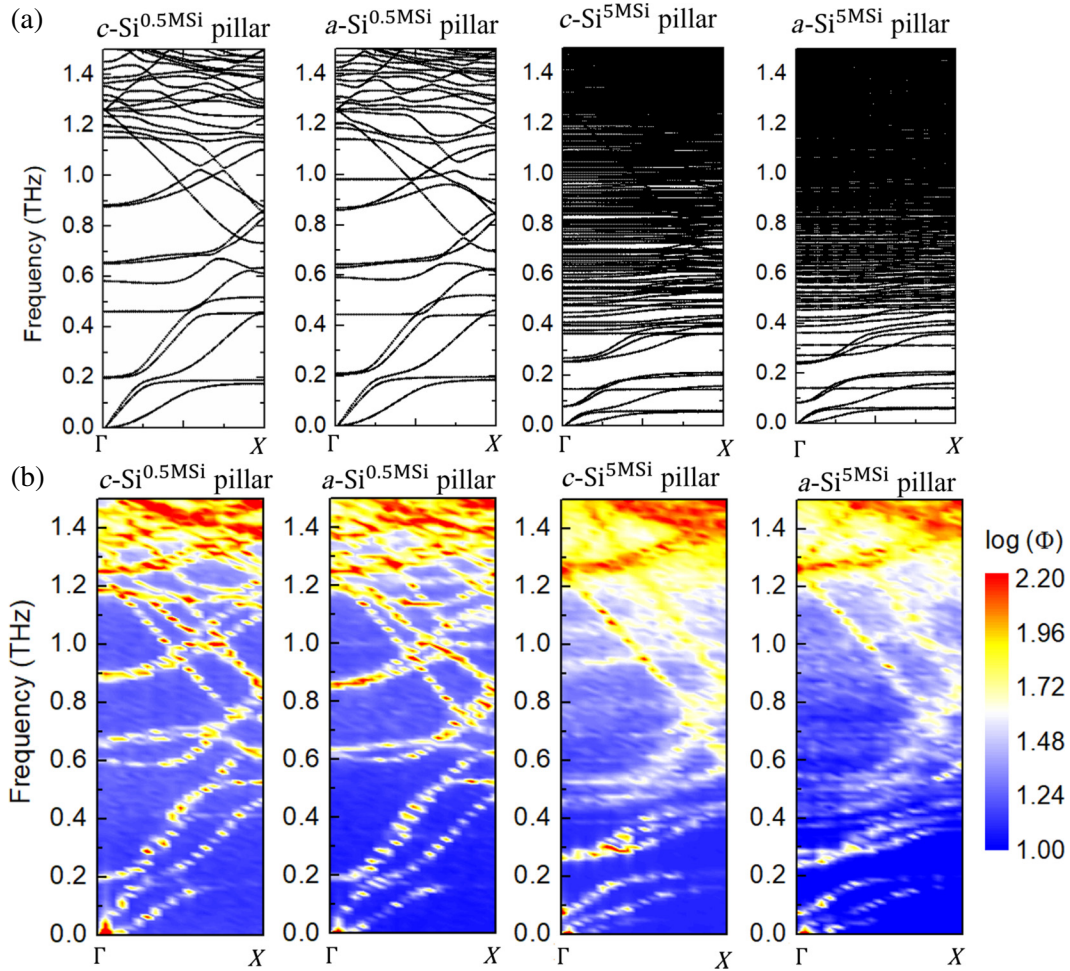


FIG. 4. (a) Phonon dispersions of the NPMs with the  $c\text{-Si}^M$  and  $a\text{-Si}^M$  pillars calculated by lattice dynamics. (b) SED spectrum of the NPMs with the  $c\text{-Si}^M$  and  $a\text{-Si}^M$  pillars, in which only the atoms in the Si membrane are considered. The value of  $M$  is set at 0.5 MSi and 5 MSi to compare the change in the phonon dispersions. Here, the  $c\text{-Si}^{0.5\text{MSi}}\text{--}0.5\text{MSi}$  and  $a\text{-Si}^{0.5\text{MSi}}$  pillars represent  $c\text{-Si}^M$  and  $a\text{-Si}^M$  pillars with  $M = 0.5$  MSi and  $c\text{-Si}^{5\text{MSi}}$  and the  $a\text{-Si}^{5\text{MSi}}$  pillar signify the  $c\text{-Si}^M$  and  $a\text{-Si}^M$  pillars with  $M = 5$  MSi.

## B. Anomalous thermal conductivity of NPMs

The frequency of vibrational modes of the pillar can be controlled by varying its atomic mass. Additionally, it was reported that changing the atomic mass of the pillar can also weaken the resonant hybridization and abnormally increase the  $\kappa$  [25]. To further study the effect of the atomic mass, the thermal conductivity of the NPM with the  $c\text{-Si}^M$  and  $a\text{-Si}^M$  pillars is calculated, where the value of  $M$  is varied from 0.5 MSi to 10 MSi. Here, when the atomic mass of atoms in pillars is changed to  $M$  in units of amu, it is denoted as the  $c\text{-Si}^M$  and  $a\text{-Si}^M$  pillars. The thermal conductivity of the NPM is normalized by the  $\kappa$  of the Si membrane, which is shown in Fig. 3(a), while the  $\kappa$  of the NPMs versus time is shown in Fig. S3 in the Supplemental Material [42]. For the NPM with the  $c\text{-Si}^M$  pillar,  $\kappa$  is the smallest when  $M$  equals MSi, and largely increases as  $M$  grows from MSi to 10 MSi, which is consistent with the findings of the graphene NPM with a larger mass

pillar [24,25]. Similarly, the NPM with the  $a\text{-Si}^M$  pillar has a larger  $\kappa$  when  $M$  is decreased from MSi to 0.5 MSi. However, its  $\kappa$  is almost unchanged as  $M$  increases from MSi to 10 MSi. The different trends of the  $\kappa$  of the NPMs as  $M$  increases in Fig. 3(a) indicates that the mechanism of reduction of  $\kappa$  is different for NPMs with the  $c\text{-Si}^M$  pillar and NPMs with the  $a\text{-Si}^M$  pillar.

To understand the different behavior of  $\kappa$  between NPM with the  $c\text{-Si}^M$  and  $a\text{-Si}^M$  pillars as  $M$  increases from MSi to 10 MSi, the density of states (DOS) in Fig. 3(b) and spectral  $\kappa$  in Figs. 3(c) and 3(d) are calculated. Figure 3(c) shows that, for the NPM with the  $c\text{-Si}^M$  pillar, the spectral  $\kappa$  contributed by the low-frequency phonon ( $< 2$  THz) is decreased due to the stronger hybridization at the low-frequency as  $M$  increases (shown in Fig. 4), while the spectral  $\kappa$  contributed by a phonon with frequency from 4.5 to 7.5 THz is increased, leading to the increase of  $\kappa$ . Figure 3(d) shows that, in the NPM with the  $a\text{-Si}^M$  pillar,

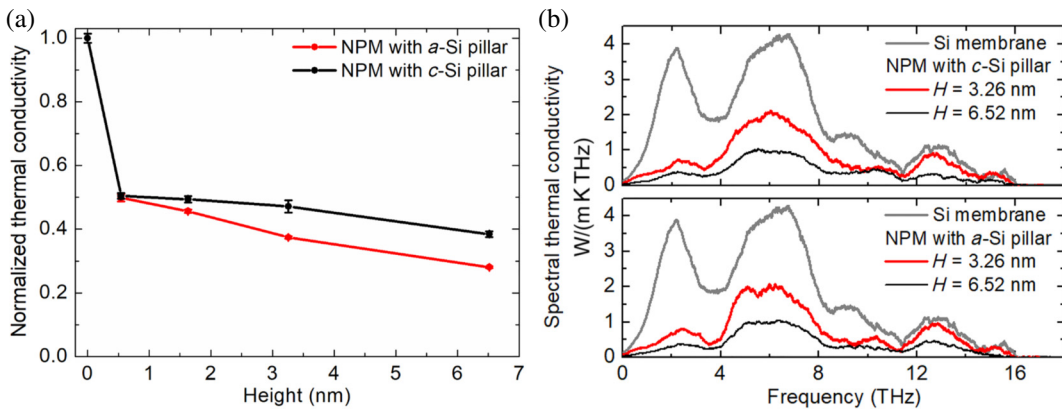


FIG. 5. (a) Normalized thermal conductivity of the NPM with the *c*-Si and *a*-Si pillars versus the height of the pillars. (b) Spectral thermal conductivity of the NPM with the *c*-Si and *a*-Si pillars for the pillar heights of 3.26 nm and 6.52 nm.

the spectral  $\kappa$  decreases as  $M$  increases for low-frequency phonons ( $< 3.5$  THz) and, for other frequency ranges, it does not show obvious trends as  $M$  increases.

The DOS in Fig. 3(b) shows that the vibrational frequencies of the *c*-Si<sup>M</sup> and *a*-Si<sup>M</sup> pillars are suppressed toward a low frequency as  $M$  increases. For example, the range of frequency of the vibrational modes is suppressed to  $\sim 7.0$  THz and  $5.0$  THz as  $M$  increases from MSi to 5 MSi and 10 MSi, respectively. Therefore, there will be fewer resonant hybridizations above  $\sim 7.0$  THz and  $\sim 5.0$  THz in the NPMs, which means that the range of frequency of resonant hybridization is reduced as  $M$  increases. In addition, changing the atomic mass of the pillar can weaken the resonant hybridizations [25]. Therefore, the  $\kappa$  of the NPM with the *c*-Si<sup>M</sup> pillar is increased as  $M$  increases due to the weakened resonant hybridizations and the reduced frequency range of resonant hybridizations. The accumulated thermal conductivity of the Si membrane versus frequency is shown in Fig. S6(a), and the DOS of the *c*-Si<sup>10MSi</sup> and *a*-Si<sup>10MSi</sup> pillars is shown in Fig. S6(b) in the Supplemental Material [42]. The contribution of the phonons with a frequency smaller than 5.0 THz is 38% in the Si membrane in Fig. S6(a) in the Supplemental Material [42]. If these phonons were completely impeded because of the resonant hybridization mechanism in the NPM with the *c*-Si<sup>10MSi</sup> pillar, the reduction of  $\kappa$  would be 38%. Additionally, these phonons could not be completely impeded, which is shown in Fig. 4; therefore, the reduction of the  $\kappa$  of the NPM with the *c*-Si<sup>10MSi</sup> pillar due to resonant hybridization should be smaller than 38%. However, the  $\kappa$  of the NPM with the *c*-Si<sup>10MSi</sup> pillar is reduced by 39%, which implies that both the resonant hybridization and scattering mechanisms have a substantial contribution to the reduction of the  $\kappa$  of the NPM with the *c*-Si pillar. Similarly, a previous work quantified the particle and wave effects on the reduction of  $\kappa$  of one type of NPM (the Si nanowire cross junction). By combining Monte Carlo and atomic Green's function methods, it was found that the particle effect is also quite significant

and can contribute as much as 39% to the total reduction of  $\kappa$ , highlighting the importance of the mutual particle and wave effects in the NPMs [51].

On the other hand, the  $\kappa$  of the NPM with the *a*-Si<sup>M</sup> pillar is almost unchanged as  $M$  increases, which implies that the phonon scatterings at the interface between the *a*-Si<sup>M</sup> pillar and the Si membrane dominate the suppression of the phonon transport. Furthermore, the value of  $M$  is set at 0.5 MSi and 5 MSi to compare the change of the phonon dispersion of the NPMs in Fig. 4(a). Here, the *c*-Si<sup>0.5MSi</sup> and *c*-Si<sup>5MSi</sup> pillars represent the *c*-Si<sup>M</sup> pillar with  $M = 0.5$  MSi and 5 MSi, respectively; the *a*-Si<sup>0.5MSi</sup> and *a*-Si<sup>5MSi</sup> pillars are treated analogously. The corresponding SED spectrum only includes the atoms in the Si membrane, as shown in Fig. 4(b). The SED spectrum that includes all the atoms in the NPMs is shown in Fig. S4 in the Supplemental Material [42]. For  $M = 0.5$  MSi, there are fewer vibrational modes in the NPMs with crystalline and amorphous pillars compared with the NPMs with  $M = \text{MSi}$  [Fig. 2(a), Type 3 and Type 4]. In addition, the frequency of the first hybridization moves from 0.15 THz in Fig. 2(a) for Type 3 and Type 4 to  $\sim 0.2$  THz in Fig. 4(a) for  $M = 0.5$  MSi. These phenomena imply that the local resonant hybridization should be weakened, which in turn results in a larger  $\kappa$  compared with the NPM with  $M = \text{MSi}$ . For  $M = 5$  MSi, the frequency of the first hybridization moves to  $\sim 0.07$  THz. However, the phonon dispersions from 0.7 to 1.4 THz are not severely changed, as shown in Fig. 4(b), although the vibrational modes of the pillar are very dense.

### C. Pillar height effect on the thermal conductivity of NPMs

Besides different materials for the pillars, the height ( $H$ ) of the pillars is another factor in tuning the  $\kappa$  of the NPMs [9]. Here, the pillars with heights of  $H = 0.54$ ,  $1.63$ ,  $3.26$ , and  $6.52$  nm are examined. The  $\kappa$  of the NPMs with the

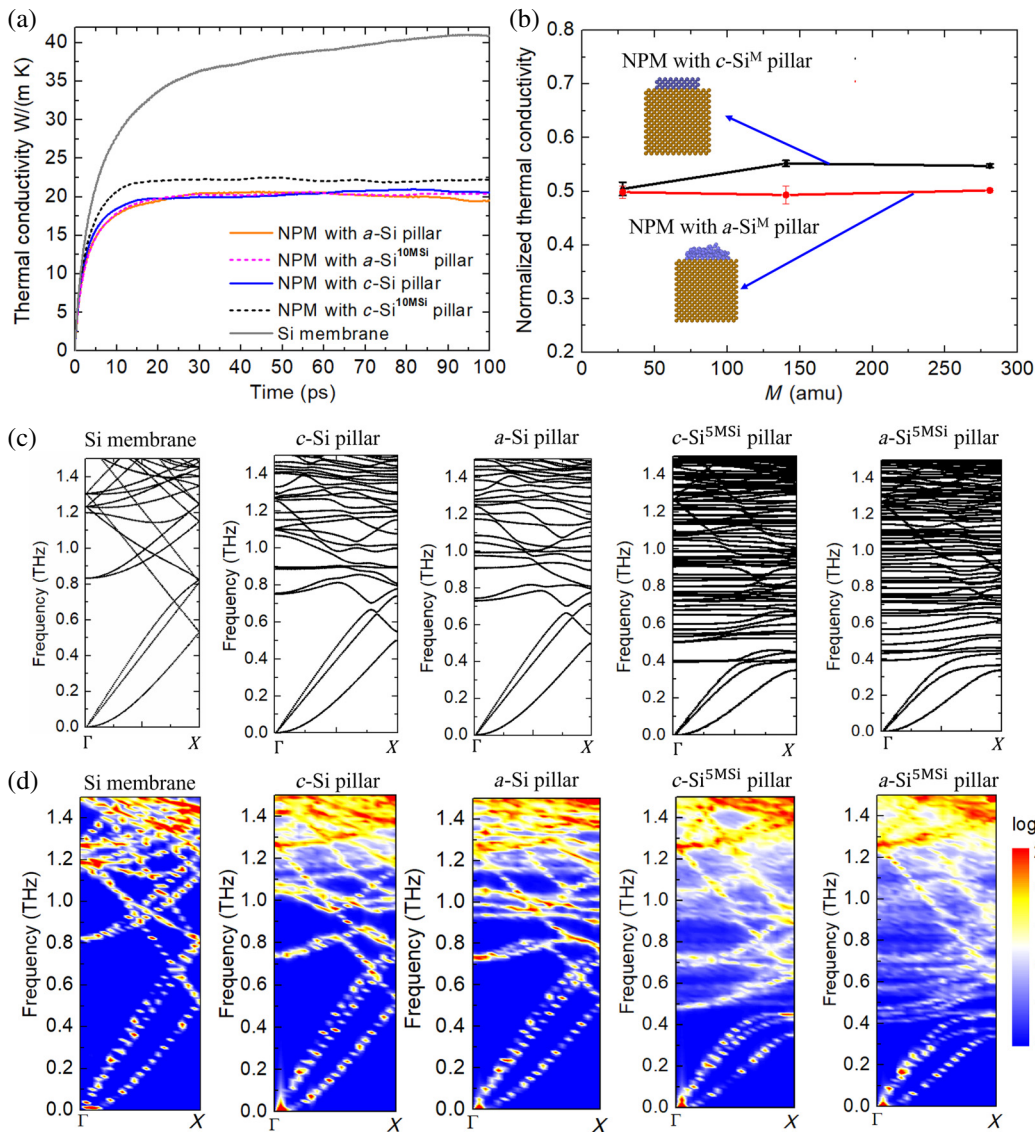


FIG. 6. (a) Thermal conductivity of the NPMs with the short crystalline pillar and the NPMs with the short amorphous pillar versus time. The height of the pillars is  $H = 0.54$  nm. (b) Normalized thermal conductivity of the NPM with the short  $c$ -Si<sup>M</sup> and short  $a$ -Si<sup>M</sup> pillars versus the value of  $M$ . The thermal conductivity of the NPM is normalized by the  $\kappa$  of the Si membrane. (c) Phonon dispersions of the Si membrane and the NPMs calculated using lattice dynamics. (d) SED spectrum of the Si membrane and the NPMs when only considering atoms in the Si membrane. In (c) and (d), the  $M$  is set at 5 MSi for the NPM with the  $c$ -Si<sup>M</sup> pillar and the NPM with the  $a$ -Si<sup>M</sup> pillar.

$c$ -Si and  $a$ -Si pillars versus height are shown in Fig. 5(a). Furthermore, the spectral  $\kappa$  of the NPMs are calculated in Fig. 5(b). For short pillars (i.e.,  $H = 0.54$  nm), the  $\kappa$  of the NPMs with the  $c$ -Si pillar is close to that of the NPM with the  $a$ -Si pillar, while  $\kappa$  is largely reduced by 61% for the  $c$ -Si pillar and 72% for the  $a$ -Si pillar as the height increases to 6.52 nm, which is consistent with previous reports [13,39]. Moreover, the  $a$ -Si pillars cause a larger reduction of  $\kappa$  compared with the corresponding  $c$ -Si pillar for each pillar height case. Further analyses show that the spectral  $\kappa$  of the NPMs is reduced in the whole frequency range as the height of the pillar increases, as shown in Fig. 5(b).

#### D. Thermal conductivity of NPMs with short pillars

Finally, the effect of the atomic mass on the  $\kappa$  of the NPMs with short pillars is investigated. The height of the short pillar is 0.54 nm. The  $\kappa$  of the NPMs with short crystalline pillar and short amorphous pillar versus time is shown in Fig. 6(a). Figure 6(b) shows the  $\kappa$  of the NPM with the short  $c$ -Si<sup>M</sup> and short  $a$ -Si<sup>M</sup> pillars versus the value of  $M$ . It is found that  $\kappa$  is changed only by  $\sim 4.3\%$  for the NPM with the short  $c$ -Si<sup>M</sup> pillar as  $M$  increases from MSi to 10 MSi, while  $\kappa$  is changed by 17% for the NPM with the  $c$ -Si<sup>M</sup> pillar in Fig. 3(a). Therefore, the  $\kappa$  of the NPM with the short  $c$ -Si<sup>M</sup> pillar is less sensitive

to the change in the atomic mass, which means that the resonant hybridization mechanism is much weaker in the NPMs with the short crystalline pillar. Additionally, the  $\kappa$  of the NPM with the short  $a\text{-Si}^M$  pillar is almost unchanged as the value of  $M$  increases, which is the same as that in Fig. 3(a) for the NPM with the  $a\text{-Si}^M$  pillar. These results indicate that the resonant hybridization mechanism is weak on reducing the  $\kappa$  of the NPM with the short  $c\text{-Si}$  pillar, and scatterings dominate on the reduction of the  $\kappa$  of both the NPM with the short  $c\text{-Si}$  and short  $a\text{-Si}$  pillars.

Furthermore, the phonon dispersions of the NPMs with short pillars are calculated using lattice dynamics, and the SED spectrum of the NPMs with the short pillars that only consider atoms in the Si membrane are also investigated, which are shown in Figs. 6(c) and 6(d). Compared with Figs. 2 and 4, there are a smaller number of resonant hybridizations. This is because the short pillars have a smaller number of atoms; thus, a smaller number of vibrational modes can be introduced. Therefore, the hybridization mechanism is weaker in the NPMs with the short pillars compared with the NPMs with the higher pillars, which is consistent with the analyses of thermal conductivity in Figs. 6(a) and 6(b).

Moreover, the difference between the Si membrane with the pillars and the Si membrane with the layers is investigated, which is shown in Figs. S7–S9 in the Supplemental Material [42]. The spatial distribution for the pillars and the layers is different. In the NPMs, these pillars are discretely distributed, and the heat flux cannot directly transport between the adjacent pillars. However, the layers are continuously distributed on the surface of the Si membrane, and the heat flux can be directly transported within the layers. The difference in the spatial distribution of the pillars and layers may cause a different effect on altering the thermal conductivity of the Si membrane.

#### IV. CONCLUSIONS

In this work, the thermal conductivity of the NPM with the crystalline Si pillar, the crystalline Ge pillar, and the amorphous Si pillar are systematically investigated using MD simulations. The phonon dispersion and spectral energy density show that the phonon dispersions are flattened due to local resonant hybridization induced by both the crystalline pillar and the amorphous pillar. In addition, the  $a\text{-Si}$  pillar can cause a larger reduction in thermal conductivity compared with the  $c\text{-Si}$  pillar. Moreover, the thermal conductivity of the NPM with the crystalline Si pillar is increased as the atomic mass of the atoms in the pillar increases because of the weakened resonant hybridization. However, the thermal conductivity of the NPM with the amorphous Si pillar is almost unchanged as the atomic mass of the atoms in the pillar increases. The analyses of the reduction of the thermal conductivity show that both the resonant hybridization and scattering

mechanisms are important in the NPM with the crystalline pillar, while the scattering mechanism dominates in both the NPM with the amorphous pillar and NPM with the short crystalline pillar. Furthermore, the thermal conductivity of the NPM decreases as the pillar height increases for both the crystalline pillar and the amorphous pillar. For various applications requiring tailored thermal properties, the results of this work show that the thermal conductivity of the NPMs can be tuned through the choice of pillar materials and their heights.

#### ACKNOWLEDGMENTS

This work was sponsored by the Beijing Institute of Technology Research Fund Program for Young Scholars (L.Y.).

- [1] J. Chen, X. Xu, J. Zhou, and B. Li, Interfacial thermal resistance: Past, present, and future, *Rev. Mod. Phys.* **94**, 025002 (2022).
- [2] C. Li, J. Wang, Y. Sheng, L. Yang, and Y. Su, The strain-dependent interfacial thermal resistance at graphene-silicon interface under various deformation conditions, *Int. J. Heat Mass Transfer* **198**, 123383 (2022).
- [3] Z. Tian, S. Lee, and G. Chen, Heat transfer in thermoelectric materials and devices, *J. Heat Transfer* **135**, 061605 (2013).
- [4] Q. Yan and M. G. Kanatzidis, High-performance thermoelectrics and challenges for practical devices, *Nat. Mater.* **21**, 503 (2022).
- [5] L. Yang, N. Yang, and B. Li, Thermoelectric properties of nanoscale three dimensional Si phononic crystals, *Int. J. Heat Mass Transfer* **99**, 102 (2016).
- [6] B. L. Davis and M. I. Hussein, Nanophononic metamaterial: Thermal conductivity reduction by local resonance, *Phys. Rev. Lett.* **112**, 055505 (2014).
- [7] S. Xiong, K. Sääskilahti, Y. A. Kosevich, H. Han, D. Donadio, and S. Volz, Blocking phonon transport by structural resonances in alloy-based nanophononic metamaterials leads to ultralow thermal conductivity, *Phys. Rev. Lett.* **117**, 025503 (2016).
- [8] K. Ren, X. Liu, S. Chen, Y. Cheng, W. Tang, and G. Zhang, Remarkable reduction of interfacial thermal resistance in nanophononic heterostructures, *Adv. Funct. Mater.* **30**, 2004003 (2020).
- [9] M. I. Hussein, C. N. Tsai, and H. Honarvar, Thermal conductivity reduction in a nanophononic metamaterial versus a nanophononic crystal: A review and comparative analysis, *Adv. Funct. Mater.* **30**, 1906718 (2020).
- [10] R. Anufriev, J. Maire, and M. Nomura, Review of coherent phonon and heat transport control in one-dimensional phononic crystals at nanoscale, *APL Mater.* **9**, 070701 (2021).
- [11] R. Anufriev and M. Nomura, Phonon and heat transport control using pillar-based phononic crystals, *Sci. Technol. Adv. Mater.* **19**, 863 (2018).

- [12] Z. Zhang, Y. Guo, M. Bescond, J. Chen, M. Nomura, and S. Volz, Heat conduction theory including phonon coherence, *Phys. Rev. Lett.* **128**, 015901 (2022).
- [13] H. Honarvar and M. I. Hussein, Two orders of magnitude reduction in silicon membrane thermal conductivity by resonance hybridizations, *Phys. Rev. B* **97**, 195413 (2018).
- [14] L. Yang, N. Yang, and B. Li, Extreme low thermal conductivity in nanoscale 3D Si phononic crystal with spherical pores, *Nano Lett.* **14**, 1734 (2014).
- [15] M. Maldovan, Sound and heat revolutions in phononics, *Nature* **503**, 209 (2013).
- [16] B. T. Spann, J. C. Weber, M. D. Brubaker, T. E. Harvey, L. Yang, H. Honarvar, C.-N. Tsai, A. C. Treglia, M. Lee, and M. I. Hussein, Semiconductor thermal and electrical properties decoupled by localized phonon resonances, *Adv. Mater.* **35**, 2209779 (2023).
- [17] R. Anufriev, R. Yanagisawa, and M. Nomura, Aluminium nanopillars reduce thermal conductivity of silicon nanobeams, *Nanoscale* **9**, 15083 (2017).
- [18] J. Maire, R. Anufriev, T. Hori, J. Shiomi, S. Volz, and M. Nomura, Thermal conductivity reduction in silicon fishbone nanowires, *Sci. Rep.* **8**, 4452 (2018).
- [19] R. Anufriev and M. Nomura, Coherent thermal conduction in silicon nanowires with periodic wings, *Nanomaterials* **9**, 142 (2019).
- [20] S. Neogi, J. S. Reparaz, L. F. C. Pereira, B. Graczykowski, M. R. Wagner, M. Sledzinska, A. Shchepetov, M. Prunnila, J. Ahopelto, and C. M. Sotomayor-Torres, Tuning thermal transport in ultrathin silicon membranes by surface nanoscale engineering, *ACS Nano* **9**, 3820 (2015).
- [21] X. Huang, D. Ohori, R. Yanagisawa, R. Anufriev, S. Samukawa, and M. Nomura, Coherent and incoherent impacts of nanopillars on the thermal conductivity in silicon nanomembranes, *ACS Appl. Mater. Interface* **12**, 25478 (2020).
- [22] C. Shao, Q. Rong, M. Hu, and H. Bao, Probing phonon–surface interaction by wave-packet simulation: Effect of roughness and morphology, *J. Appl. Phys.* **122**, 155104 (2017).
- [23] H. Zhang, B. Sun, S. Hu, H. Wang, Y. Cheng, S. Xiong, S. Volz, and Y. Ni, Novel phonon resonator based on surface screw thread for suppressing thermal transport of Si nanowires, *Phys. Rev. B* **101**, 205418 (2020).
- [24] D. Ma, X. Wan, and N. Yang, Unexpected thermal conductivity enhancement in pillared graphene nanoribbon with isotopic resonance, *Phys. Rev. B* **98**, 245420 (2018).
- [25] H. Wang, Y. Cheng, Z. Fan, Y. Guo, Z. Zhang, M. Bescond, M. Nomura, T. Ala-Nissila, S. Volz, and S. Xiong, Anomalous thermal conductivity enhancement in low dimensional resonant nanostructures due to imperfections, *Nanoscale* **13**, 10010 (2021).
- [26] A. Stukowski, Visualization and analysis of atomistic simulation data with OVITO—the Open Visualization Tool, *Modell. Simul. Mater. Sci. Eng.* **18**, 015012 (2010).
- [27] J. Tersoff, Modeling solid-state chemistry: Interatomic potentials for multicomponent systems, *Phys. Rev. B* **39**, 5566 (1989).
- [28] A. P. Thompson, H. M. Aktulga, R. Berger, D. S. Bolintineanu, W. M. Brown, P. S. Crozier, P. J. in't Veld, A. Kohlmeyer, S. G. Moore, and T. D. Nguyen, LAMMPS—a flexible simulation tool for particle-based materials modeling at the atomic, meso, and continuum scales, *Comput. Phys. Commun.* **271**, 108171 (2022).
- [29] P. K. Schelling, S. R. Phillpot, and P. Keblinski, Comparison of atomic-level simulation methods for computing thermal conductivity, *Phys. Rev. B* **65**, 144306 (2002).
- [30] K. Gordiz, D. J. Singh, and A. Henry, Ensemble averaging vs. time averaging in molecular dynamics simulations of thermal conductivity, *J. Appl. Phys.* **117**, 045104 (2015).
- [31] Z. Wang, S. Safarkhani, G. Lin, and X. Ruan, Uncertainty quantification of thermal conductivities from equilibrium molecular dynamics simulations, *Int. J. Heat Mass Transfer* **112**, 267 (2017).
- [32] J. M. Larkin and A. J. McGaughey, Thermal conductivity accumulation in amorphous silica and amorphous silicon, *Phys. Rev. B* **89**, 144303 (2014).
- [33] I. Štich, R. Car, and M. Parrinello, Amorphous silicon studied by ab initio molecular dynamics: Preparation, structure, and properties, *Phys. Rev. B* **44**, 11092 (1991).
- [34] S. Tian, T. Wu, S. Hu, D. Ma, and L. Zhang, Boosting phonon transport across AlN/SiC interface by fast annealing amorphous layers, *Appl. Phys. Lett.* **124**, 042202 (2024).
- [35] L. Yang, Y. Jiang, and Y. Zhou, Quantitatively predicting modal thermal conductivity of nanocrystalline Si by full-band Monte Carlo simulations, *Phys. Rev. B* **104**, 195303 (2021).
- [36] J. D. Gale and A. L. Rohl, The general utility lattice program (GULP), *Mol. Simul.* **29**, 291 (2003).
- [37] J. Larkin, J. Turney, A. Massicotte, C. Amon, and A. McGaughey, Comparison and evaluation of spectral energy methods for predicting phonon properties, *J. Comput. Theor. Nanosci.* **11**, 249 (2014).
- [38] J. A. Thomas, J. E. Turney, R. M. Iutzi, C. H. Amon, and A. J. McGaughey, Predicting phonon dispersion relations and lifetimes from the spectral energy density, *Phys. Rev. B* **81**, 081411 (2010).
- [39] H. Honarvar and M. I. Hussein, Spectral energy analysis of locally resonant nanophononic metamaterials by molecular simulations, *Phys. Rev. B* **93**, 081412 (2016).
- [40] Y. Zhou, X. Zhang, and M. Hu, Quantitatively analyzing phonon spectral contribution of thermal conductivity based on nonequilibrium molecular dynamics simulations. I. From space Fourier transform, *Phys. Rev. B* **92**, 195204 (2015).
- [41] Y. Xu, L. Yang, and Y. Zhou, The interfacial thermal conductance spectrum in nonequilibrium molecular dynamics simulations considering anharmonicity, asymmetry and quantum effects, *Phys. Chem. Chem. Phys.* **24**, 24503 (2022).
- [42] See Supplemental Material at <http://link.aps.org/supplemental/10.1103/PhysRevApplied.22.034016> for details about the EMD simulations for different types of NPMs, SED spectrum in NPMs, NEMD simulations, thermal conductivity of Si membrane and DOS of pillars, and Si membrane with layers.
- [43] X. Li, K. Maute, M. L. Dunn, and R. Yang, Strain effects on the thermal conductivity of nanostructures, *Phys. Rev. B* **81**, 245318 (2010).

- [44] D. P. Sellan, E. S. Landry, J. Turney, A. J. McGaughey, and C. H. Amon, Size effects in molecular dynamics thermal conductivity predictions, *Phys. Rev. B* **81**, 214305 (2010).
- [45] J.-H. Lee, J. Grossman, J. Reed, and G. Galli, Lattice thermal conductivity of nanoporous Si: Molecular dynamics study, *Appl. Phys. Lett.* **91**, 223110 (2007).
- [46] E. Chávez-Angel, J. S. Reparaz, J. Gomis-Bresco, M. R. Wagner, J. Cuffe, B. Graczykowski, A. Shchepetov, H. Jiang, M. Prunnila, and J. Ahopelto, Reduction of the thermal conductivity in free-standing silicon nano-membranes investigated by non-invasive Raman thermometry, *APL Mater.* **2**, 012113 (2014).
- [47] C. J. Glassbrenner and G. A. Slack, Thermal conductivity of silicon and germanium from 3 K to the melting point, *Phys. Rev.* **134**, A1058 (1964).
- [48] J. Turney, A. McGaughey, and C. Amon, Assessing the applicability of quantum corrections to classical thermal conductivity predictions, *Phys. Rev. B* **79**, 224305 (2009).
- [49] M. Hu and D. Poulikakos, Si/Ge superlattice nanowires with ultralow thermal conductivity, *Nano Lett.* **12**, 5487 (2012).
- [50] S. Xiong, D. Sellli, S. Neogi, and D. Donadio, Native surface oxide turns alloyed silicon membranes into nanophononic metamaterials with ultralow thermal conductivity, *Phys. Rev. B* **95**, 180301 (2017).
- [51] D. Ma, A. Arora, S. Deng, G. Xie, J. Shiomi, and N. Yang, Quantifying phonon particle and wave transport in silicon nanophononic metamaterial with cross junction, *Mater. Today Phys.* **8**, 56 (2019).